Geochemistry, Geophysics, Geosystems®

RESEARCH ARTICLE
10.1029/2026GC012967

Borehole Waters From Hole U1601C (Atlantis Massif) Provide Constraints for a Deep-Sourced Formation Water That (Could) Feed the Lost City Hydrothermal Field

C. Geoffrey Wheat[1], Susan Q. Lang[2], Gordon Southam[3], Will Osborne[4], Ivan P. Savov[4,5], Samuele Agostini[5], and Jordan Poitras[6]

[1]Global Undersea Research Unit, University of Alaska Fairbanks, Moss Landing, CA, USA, [2]Departments of Geology and Geophysics, Woods Hole Oceanographic Institution, Woods Hole, MA, USA, [3]School of the Environment and Sustainable Minerals Institute, University of Queensland, St. Lucia, QLD, Australia, [4]School of Earth and Environment, University of Leeds, Leeds, UK, [5]Istituto di Geoscienze e Georisorse, Consiglio Nazionale delle Ricerche, Area della Ricerca di Pisa, Pisa, Italy, [6]Centre for Microscopy and Microanalysis & School of the Environment, University of Queensland, St. Lucia, QLD, Australia

Key Points:

- International Ocean Discovery Program Hole U1601C drilled 1,268 m of mantle rocks at Atlantis Massif near the Lost City Hydrothermal Field
- Systematic variations in solute concentrations and isotope values reveal borehole waters with multiple sources, including formation water
- Formation waters suggest interaction with gabbroic rocks, lending credibility to a deep origin for Lost City's alkaline hydrothermal fluid

Supporting Information:

Supporting Information may be found in the online version of this article.

Correspondence to:

C. G. Wheat,
cgwheat@alaska.edu

Citation:

Wheat, C. G., Lang, S. Q., Southam, G., Osborne, W., Savov, I. P., Agostini, S., & Poitras, J. (2026). Borehole waters from Hole U1601C (Atlantis Massif) provide constraints for a deep-sourced formation water That (could) feed the Lost City Hydrothermal Field. *Geochemistry, Geophysics, Geosystems*, *27*, e2026GC012967. https://doi.org/10.1029/2026GC012967

Received 30 JAN 2026
Accepted 28 MAY 2026

Author Contributions:

Conceptualization: C. Geoffrey Wheat
Data curation: C. Geoffrey Wheat
Formal analysis: C. Geoffrey Wheat, Susan Q. Lang, Gordon Southam, Will Osborne, Ivan P. Savov, Samuele Agostini, Jordan Poitras
Funding acquisition: C. Geoffrey Wheat, Susan Q. Lang, Gordon Southam, Ivan P. Savov
Methodology: C. Geoffrey Wheat, Susan Q. Lang, Gordon Southam, Will Osborne,

Abstract Hole U1601C, drilled during International Ocean Discovery Program (IODP) Expedition 399, reached a depth of 1,268 m below the seafloor (mbsf) in the Atlantis Massif (30°N, 42°W). This borehole represents only one of six boreholes that extends more than 700 m into oceanic rock, penetrating predominantly ultramafic lithologies, mostly composed of variously altered serpentinized peridotite and gabbro. We report geochemical data from borehole water collected after drilling and logging operations, providing a unique opportunity to investigate water–rock and hydrologic interactions and their implications for the origin of hydrothermal fluids at the Lost City Hydrothermal Field (LCHF), ~800 m to the south. Solute concentrations and isotope compositions reveal trends consistent with four-component mixing. Borehole waters are a mixture of surface seawater used during drilling, freshwater introduced before logging, bottom seawater that entered after drilling, and formation water, which discharges into the base of the borehole. The upper 465 m of the borehole is dominated by seawater-freshwater mixtures, whereas deeper intervals contain increasing proportions of a zero-Mg, high-Ca formation water that constitutes up to 80% of the deepest samples. This formation water reacted with gabbroic and peridotite lithologies at temperatures ≥300°C, enriching the water in Ca, Li, Rb, Cs, and Sr. These findings are similar to models of deep-sourced hydrothermal fluids that discharge from LCHF. Our results provide the first direct evidence for deep, high-temperature fluid circulation through gabbroic and ultramafic lithologies beneath the Atlantis Massif and elucidate subsurface hydrologic processes that source Lost City's unique hydrothermal fluids.

Plain Language Summary Scientists drilled a 1,268-m-deep borehole into the Atlantis Massif, near the Lost City Hydrothermal Field in the Atlantic Ocean. This borehole is significant because we were able to recover mostly mantle rocks called peridotites, which normally lie very deep beneath the seafloor and are rarely available for direct study. After drilling, water from the borehole was collected and analyzed to understand how seawater moves through and reacts with the rock, altering both. Borehole waters are a mixture of seawater, drilling-related freshwater, and a natural water that discharges from deep within the borehole. This natural water equilibrated with hot mantle and gabbroic rocks at high temperatures ≥300°C and is similar in composition to hydrothermal fluids that discharge at Lost City, one of Earth's most unique hydrothermal systems. These findings demonstrate how seawater circulates deep into oceanic plates and transports chemical energy to shallower environments, potentially supporting microbial life.

1. Introduction

Chemical reactions between seawater and mantle rocks are a fundamental planetary process that regulates ocean chemistry, provides energy for deep-sourced microbial ecosystems, and serves as a model for the potential habitability of icy moons. However, despite its global importance, our direct access to the deep ocean basement is severely limited. Five decades of scientific ocean drilling have yielded only six boreholes that have penetrated more than 700 m of rock (Lang, McCaig, et al., 2025; Michibayashi et al., 2019). Rock (core) samples recovered from these uniquely deep boreholes have proven exceptionally informative, yielding foundational data on sub-seafloor composition, alteration, and hydrology (e,g., Alt et al., 1986; Ildefonse et al., 2007; Carlson, 2010;

10.1029/2026GC012967

Ivan P. Savov, Samuele Agostini, Jordan Poitras
Writing – original draft: C. Geoffrey Wheat
Writing – review & editing: Susan Q. Lang, Gordon Southam, Will Osborne, Ivan P. Savov, Jordan Poitras

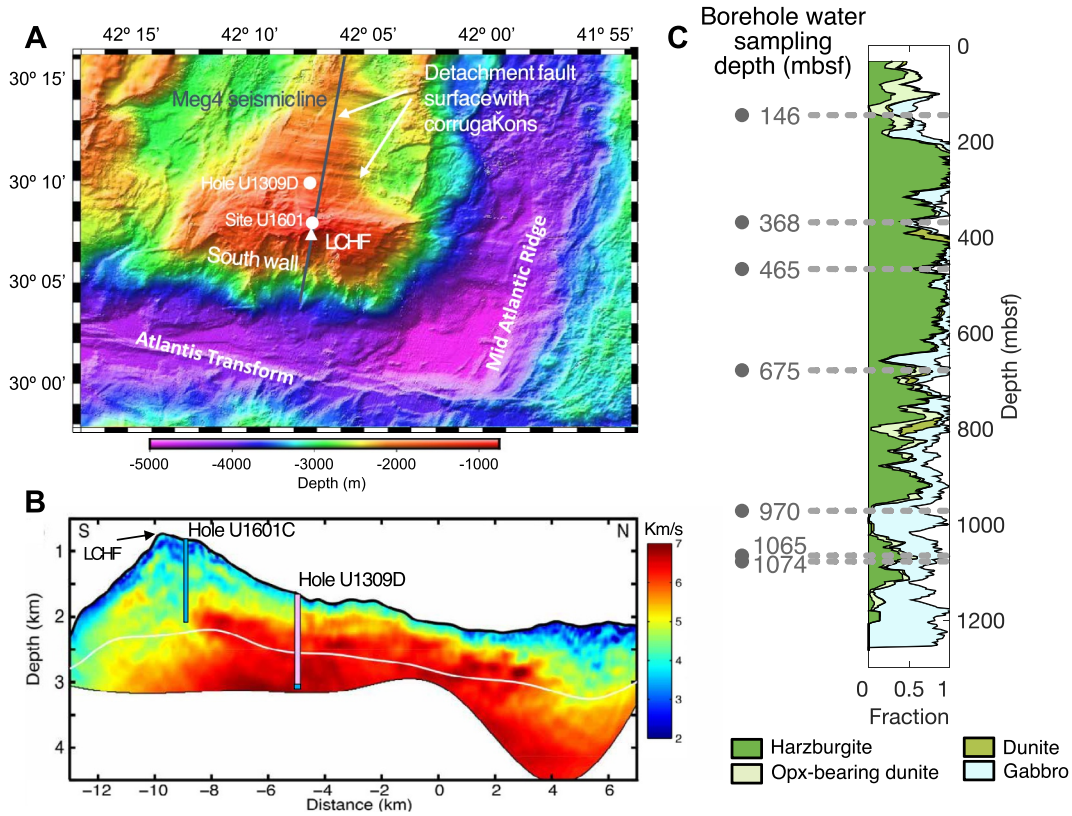

Figure 1. (a) Bathymetric map of the Atlantis Massif indicating the location of Site U1601, Hole U1309D, and the Lost City hydrothermal field (LCHF); adapted from Früh-Green et al. (2017). (b) Seismic line Meg 4 with locations of the newly drilled Hole U1601C and Hole U1309D; adapted from Harding et al. (2016). The high velocity gabbroic rock penetrated by Hole U1309D (red) contrasts with the mostly serpentinized peridotite at Hole U1601C. (c) Downhole lithology of recovered material from Hole U1601C highlights the depths from which water samples were collected within the borehole (Credit: Kuan-Yu Lin).

Gilbert & Salisbury, 2011; Blackman et al., 2011; Gillis et al., 2014). However, to fully constrain these processes, we must also understand active water-rock reactions and hydrologic mechanisms (e.g., Magenheim & Gieskes, 1996; Mottl & Gieskes, 1990; Wheat et al., 2004) that drive large-scale geochemical changes among Earth's reservoirs.

During International Ocean Discovery Program (IODP) Expedition 399 (McCaig et al., 2024), the sixth deep borehole (U1601C) was drilled at the Atlantic Massif (30°N, 42°W) to a depth of 1,268 m below the seafloor (mbsf) (Lang, McCaig, et al., 2025). This is the first oceanic borehole that penetrated primarily ultramafic rock, but with considerable gabbroic intervals (Lissenberg et al., 2024). Hole U1601C was strategically located 800 m north of the Lost City Hydrothermal Field (LCHF) (Figure 1), a key site for elucidating the effects of serpentinization within peridotites (Kelley et al., 2005). Here, peridotites are exhumed at slow (2.5 cm/yr full rate) spreading ridges, which account for up to 50% of the global length of spreading ridges on Earth (Escartín et al., 2008; Pariso et al., 1996). This new borehole compliments and expands efforts from a nearby (~5 km) borehole U1309D, which penetrated 1,498 m of mostly gabbroic rocks (Blackman et al., 2006; McCaig et al., 2024), and 17 shorter (1–16 m) boreholes that were drilled on IODP Exp. 357 (Früh-Green et al., 2017) that provide a regional context for rock type and alteration. Combined, data from these boreholes provide a record of alteration and deformation associated with detachment faulting responsible for exhumation of the massif and reveal a complex, heterogeneous rock structure through which seawater flows (channelized to pervasive), altering the rock matrix on a range of time scales (Früh-Green et al., 2017, 2018).

The Atlantic Massif records various stages of rock alterations due to seawater infiltration, water-rock interactions, and evolution. One fluid pathway results in a high pH (>10) and warm (>70°C) altered hydrothermal fluid that discharges through carbonate and brucite chimneys that rise 30–60 m above the seafloor (Kelley et al., 2005).

Models for the subseafloor flow path suggest a multi-stage process. The first stage includes infiltrated seawater that is warm (>150°C) and reacts within the rock formation at depth (e.g., Delacour, Früh-Green, & Bernasconi, 2008; Delacour, Früh-Green, Frank, et al., 2008; Evans et al., 2024; Foustoukos et al., 2008; Seyfried et al., 2015). Additional stages include further water-rock reactions as the altered seawater ascends along a tortuous path. During its ascent, the altered seawater potentially mixes with descending/intruded seawater in the subseafloor, is cooled conductively, and is a source for microbial metabolic processes that further alter some solute concentrations (e.g., Aquino et al., 2024; Lang, Wheat, et al., 2025; Lang et al., 2012).

This study reports the chemical composition of waters from Hole U1601C, sampled days after the initial drilling to a depth of 1182.2 mbsf; additional drilling occurred after water samples were collected. Collected waters were a mixture of four sources: surface seawater, which was used as a drilling water to clear cuttings from the borehole, freshwater used to flush the borehole prior to logging operations, bottom seawater that mixed with borehole water after drilling operations ceased, and a (deep) metamorphic basement water (herein referred to as the formation water) that discharged into the deepest portions of the borehole and may discharged in shallower portions of the borehole. Complicating the partitioning of these sources is the reaction of some solutes in the borehole between the time of the freshwater flush and sample collection. By chemically disentangling these inputs and accounting for their subsequent alteration reactions within the borehole, we identified and characterized the natural high-temperature (>150°C) formation water. A comparison with hydrothermal fluids from the LCHF suggests this formation water may represent the deep-sourced geochemical endmember that feeds the LCHF.

2. Methods

2.1. Borehole Operations

We summarize relevant drilling operations that set the stage for borehole water sampling operations, the focus of this contribution. Extensive operational notes are presented in Lang, McCaig, et al. (2025). Hole U1601C was initially drilled with a 1434-inch bit to a depth of ∼22 mbsf. Then, the borehole was reentered with a 978-inch coring bit. A casing-cone assembly was constructed around the drilling assembly, released, and fell into the borehole, serving as a guide for subsequent reentry operations. As a result, only the upper ∼23 m of the borehole is cased, and the remainder is open to the formation.

The recovered rock cores consisted of serpentinized mantle peridotite interleaved with gabbroic intrusions (Lissenberg et al., 2024). Gabbroic rocks become more prominent below 640 mbsf, and dominant below ∼950 mbsf. Borehole logging and water collection operations commenced when the Hole was drilled to a depth of 1182.2 mbsf. After borehole water sampling operations, the borehole was deepened to 1268 mbsf. Waters collected from core catchers indicate the presence of dissolved hydrogen throughout the borehole and carbon monoxide (CO) at deeper depths, the latter potentially associated with gabbroic intrusions (Lang, Wheat, et al., 2025). Potential drilling impacts on the subseafloor hydrologic system included regular flushing of the borehole with surface seawater and sepiolite mud sweeps, the latter occurring after each ten-m advance (Lang, McCaig, et al., 2025). Both pumping and mud sweeps enhanced the removal of cuttings from the borehole.

2.2. Water Sample Operations

Detailed water sampling operations are presented in Lang, McCaig, et al. (2025) and Lang, Wheat, et al. (2025) and are synthesized here for completeness to highlight operations that impact interpretation. When drilling operations ceased at 1182.2 mbsf, the borehole was flushed with a volume of surface seawater equal to six times the hole volume and then flushed with a volume of freshwater equal to 1.5 times the hole volume to improve the resistivity contrast during wireline logging operations. These flushing steps (7.5 times the hole volume) were required to get most of the fine cuttings out of the borehole, based on repeated sampling of borehole waters from ODP Hole 504B (Mottl & Gieskes, 1990).

Water sampling operations consisted of four wireline deployments, each with two 600-ml Kuster Flow-Through Samplers (KFTSs) and an Elevated Temperature Borehole Sonde (ETBS). A conductivity-temperature-depth (CTD) instrument (Minos-X; AML Oceanographic) was included on the first and shallowest deployment and then removed on subsequent deployments to avoid potentially excessive heat that could damage the CTD during deeper deployments. The CTD has a response time of seconds while the ETBS temperature sensor responds in

minutes. The lag in the ETBS data was demonstrated when the tool was held for 5 min at a particular depth, showing a rise in temperature (Lang, McCaig, et al., 2025).

Prior to deployment, KFTSs were serviced (e.g., valves and o-rings), cleaned with ACS reagent grade acetone, and rinsed with deionized water. Prior to deployment in Hole U1601C, the interior was further cleaned with isopropanol and then scrubbed with a brush and Simple Green soap, followed by a Mill-Q rinse. The interiors were subsequently wiped with lint-free wipes soaked in dichloromethane, then wipes soaked in methanol, and lastly dried. The interiors were then rinsed with a 5% HCl solution followed by three rinses with sterile Milli-Q water.

For each deployment, the KFTS was lowered at 50 m/min within the drill string, then slowed to 20 m/min within the open borehole and stopped about 10 min prior to the timed mechanical release. Targeted depths were 146, 368, 465, 675 (sampled twice because of a malfunction on the first attempt), 970, 1065, and 1074 mbsf. The deepest sample contained mud from the borehole even though it was 100 m shallower than the drilled borehole.

In addition to the downhole water samples, bottom seawater was collected using 1.7 and 5 L Niskin bottles (General Oceanics), which were deployed on the Vibration Isolated Television (VIT) frame, which was lowered to within 10 m of the seafloor. Surface seawater samples were collected in a cleaned bucket off the starboard side of the ship. Freshwater that was used to flush the borehole was collected on the rig floor during pumping operations.

2.3. Chemical Analyses

Water collected in the KFTS, Niskin bottles, and bucket was immediately aliquoted through a 0.4-micron filter into a series of high-density polyethylene bottles, glass vials, and syringes for subsequent ship- and shore-based chemical and isotope analyses. Data compilations of ship and shore-based results and the standard analytical methods that were employed are presented in Lang, McCaig, et al. (2025). For completeness, we included these data and the unreported $\delta^{11}B$ and $\delta\ ^{2}H$ isotope data in Table S1.

Boron abundances and isotope ratios were measured in water samples at the Istituto di Geoscienze e Georisorse (IGG) of the Italian National Research Council (IGG-CNR) in Pisa, using a *Neptune-Plus* Multi-Collector ICP-MS. Boron extraction and purification of non-filtered and non-acidified waters followed the slightly modified method of Tonarini et al., 1997, with adaptations/details presented in McCaig et al. (2018) and Agostini et al. (2021). The dataset is reported relative to the NIST SRM 951 standard ($\delta^{11}B = 0$ ‰; Catanzaro et al., 1970). We applied a correction of +0.46‰ to all fluid samples based on our measured values ($n = 6$) for NIST SRM 951. No accompanying adjustment was made to the analytical uncertainty of our measurements.

2.4. Scanning Electron Microscope—Energy Dispersive Spectroscopy Analyses

Aliquots from Kuster samplers (9 ml) were analyzed using scanning electron microscopy (SEM) and Energy Dispersive Spectroscopy (EDS). Water samples were aliquoted into 10 ml serum bottles and fixed at sea using $2.5\%_{(aq)}$ glutaraldehyde to sterilize and preserve the samples, then sealed using a butyl stopper and Al-crimp seal to prevent oxidation during storage and transport. Samples were shaken to suspend materials (mineral and bacteria) before filtration (0.1 µm pore size filter) and then dehydrated using 25%, 50%, 75%, 100%, 100%, and 100% aqueous ethanol. Finally, filters were dried using a hexamethyldisilizane (HMDS) series with 100% ethanol (1:3, 2:2, 3:1, 4:0). Prior to microscopy, samples were placed in a vacuum oven overnight at 40°C, plasma cleaned (Evactron Plasma Cleaner), and carbon coated (Quorum Q150T carbon coater). Field Emission Scanning Electron Microscopy (FESEM) was undertaken on a JEOL-JSM—7100F at an accelerating voltage of 20 keV for back scatter and between 2 and 4 keV for secondary electron imaging with a working distance of 10 mm.

3. Results

3.1. Chemical Data

Solute concentrations plotted versus depth in the borehole reveal similar trends. Concentrations decrease from the bottom seawater compositions to a depth of 465 mbsf and then increase deeper in the borehole (Figure 2; Table S1). For example, chloride concentrations decrease from a bottom seawater value of 559–150 mM at 465 mbsf, which is a mixture of about 20% seawater and 80% freshwater. Below 465 mbsf, the chloride concentration

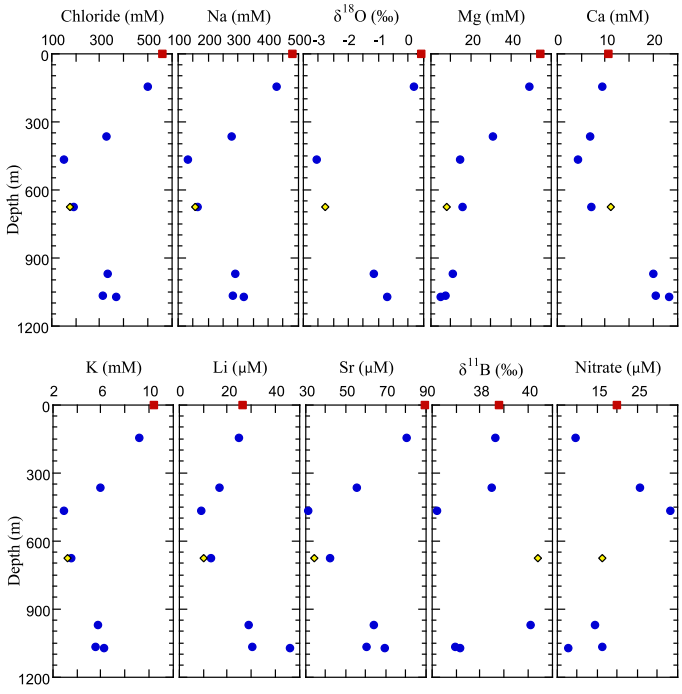

Figure 2. Concentrations of solutes (chloride, sodium, magnesium, calcium, potassium, lithium, strontium, and nitrate), water $\delta^{18}O$ isotopes, and $\delta^{11}B$ isotopes in borehole waters from Hole U1601C (blue circles). Bottom seawater is marked by a red square. Only 5% of the sample from 675 mbsf (yellow diamond) was recovered and is shown for completeness. Plots of additional solutes are shown in Figures S1 and S2 in Supporting Information S1.

increases to 367 mM in the deepest sample (1074 mbsf). Freshwater, which was pumped into the borehole prior to logging and water sampling operations, is the only water source capable of causing a significant decrease in chloride concentrations in this setting, which is well below the temperature for phase separation.

Chemical profile shapes differ among the various solutes. For example, Mg concentrations decrease at the base of the borehole, whereas concentrations of Ca increase, consistent with water-rock reactions. Further, other solutes, such as those rapidly mediated by microbial processes (e.g., nitrate, Mn, Mo, Fe, phosphate), show a range of solute-depth profiles, indicating potential reactions with newly exposed rock surfaces, drill cuttings, and sepiolite/surface seawater slurries. In addition to concentrations, isotopic compositions vary with depth. For example, $\delta^{11}B$ isotopic compositions of samples from 146 to 368 mbsf are the same as deep and surface seawater compositions; however, samples from 465mbsf and deeper display variable B isotopic compositions up to 1.5‰ above and 2.4‰ below measured seawater values (Figure 2).

3.2. Temperature and CTD Data

Multiple temperature measurements from standard borehole sensors showed a general increase with time at a particular depth, consistent with the borehole rebounding from drilling operations (Lang, Wheat, et al., 2025). Temperatures of 101–105°C were measured at 1060 mbsf. A conservative estimate of 110–140°C was calculated for the equilibrated rock temperature at 1268 mbsf, the base of the drilled borehole. Using 140°C at 1268 mbsf results in a thermal gradient of 110°C/km. This is similar to the 113°C/km gradient measured in Hole U1309, which is ∼5 km away (Blackman et al., 2014). While the temperature sensors provide fundamental data, they are not capable of revealing hydrologic changes within the borehole because of the slow (min) response time of the thermal sensors. The CTD data, with a thermal sensor response time of sec, provides a more active picture of mixing within the borehole.

The CTD was deployed on the first water sampling operation, which was within the bottom seawater-freshwater mixing zone (Table S2). The CTD was lowered to the upper sample depth and remained stationary for about 10 min to allow the mechanical clock to activate and collect a water sample. The package then descends to the depth of the lower sample, again waiting ∼10 min for the sampler to activate prior to recovering the instruments.

Temperature, salinity, and density depth-profiles from the CTD down and up casts show similar overall trends but are vertically offset (Figure 3). During the 13 min and 29 s between the up and down casts at 1100 mbsf, the thermal profile shifted upwards by 11 m (Figure 3d), consistent with the convective mixing of cooler denser bottom seawater with borehole water. Using these data, an instantaneous volumetric flux of 0.7 L/s is calculated for a hole diameter of 24.8 cm (9.75 inches). This estimate represents an upper bound, as it would overturn the entire 1,200 m borehole in ∼25 hr, which is inconsistent with the composition of the deeper samples. Alternatively, the offset could result from disturbance in the borehole from lowering the CTD in the confined borehole.

4. Discussion

4.1. Borehole Water: Multiple Component Mixing

Figure 2 shows the impact of freshwater on the chemical composition of the collected water. This impact can be "removed" by dividing solute concentrations by Cl concentrations, with the assumption that chloride is conservative in the borehole (Figure 4). For example, plots Mg/Cl and Ca/Cl show seawater ratios that persist to a depth of about 465 mbsf. At deeper depths, chemical ratios change in agreement with typical water-rock reactions, which result in a decrease in Mg/Cl ratios and an increase in Ca/Cl ratios. Such changes are consistent with a variety of alteration reactions that remove Mg from water into hydrous secondary phases and release Ca into water

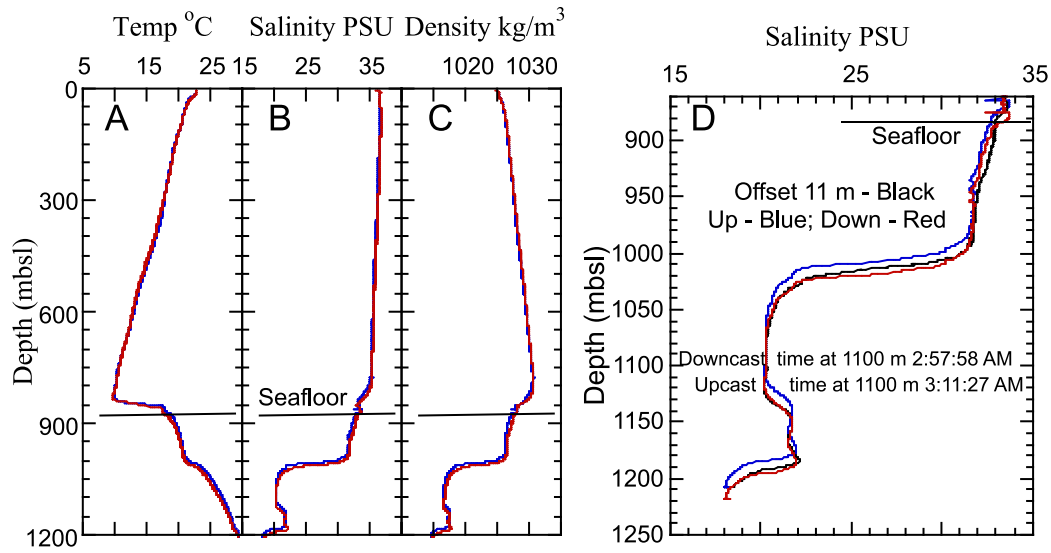

Figure 3. Depth (meters below sea level) profiles of temperature (a), salinity (conductivity) (b), and Density (c) are shown for the down (red) and up casts (blue). The horizontal line is the seafloor. (d) An expanded view of the salinity data with an additional line (black) that was calculated using data from the up cast (blue) and subtracting 11 m.

(Ligi et al., 2013). This suggests that borehole waters are derived from possibly four sources (freshwater, bottom seawater, surface seawater, and a zero-Mg water), with potential reactions further affecting concentrations of the mixture.

Three water sources are further illustrated by solute cross plots, in which two conservative mixing trends are observed for some pairs of solutes (Figure 5). For example, The Ca and Mg data highlight one trend that results from mixing bottom seawater with freshwater. This suggests that the upper ~450 m of the borehole is primarily affected by mixing warmed freshwater that was pumped into the borehole prior to logging operations with denser and colder bottom seawater. This does not preclude subsequent water-rock reactions nor the intrusion of an altered formation water at depths shallower than ~450 mbsf; however, the net effect of these processes is within the analytical uncertainty of the conservative mixing line. Similar results are observed in the Cl versus Mg plot, but the Cs versus Mg data fall off the conservative bottom seawater-freshwater mixing line, hinting at the possible addition of Cs to borehole waters in the upper zone of the borehole.

Below 465 mbsf, a second conservative mixing line is apparent (Figure 5). Ca, Cl, and Cs concentrations versus Mg data point toward the conservative mixing of a zero-Mg water and a freshwater-bottom seawater mixture. For example, the concentration of Ca for a zero-Mg water is 34 mM based on a linear regression of the five deepest samples, excluding the compromised (yellow diamond) sample. Based on these relationships, a zero-Mg water was calculated for each solute and compared to bottom seawater concentrations (Table 1). The calculated charge balance for bottom seawater is 5 mM (<1% of the Cl concentration) and 3 mM for the zero-Mg water, suggesting the major ion concentrations were determined within the scope of analytical capabilities.

4.2. Percentage of Zero-Mg Water

The percentage of the zero-Mg water, freshwater, and bottom seawater was calculated using three equations and three unknowns. Two equations are defined by solutes. We used Ca, sulfate, K, Li, and Rb to provide a range of solute types and concentrations. For example, the equation for Ca is:

$$X\,\mathrm{Ca}_{\text{rock altered}} + A\,\mathrm{Ca}_{\text{bottom seawater}} + B\,\mathrm{Ca}_{\text{fresh water}} = \mathrm{Ca}_{\text{sample}} \quad (1)$$

where X is the fraction of zero-Mg water, A is the fraction of bottom seawater and B is the fraction of freshwater. Analogous equations exist for the other solutes. A third equation is:

$$X + A + B = 1 \text{ or } B = 1 - X - A \quad (2)$$

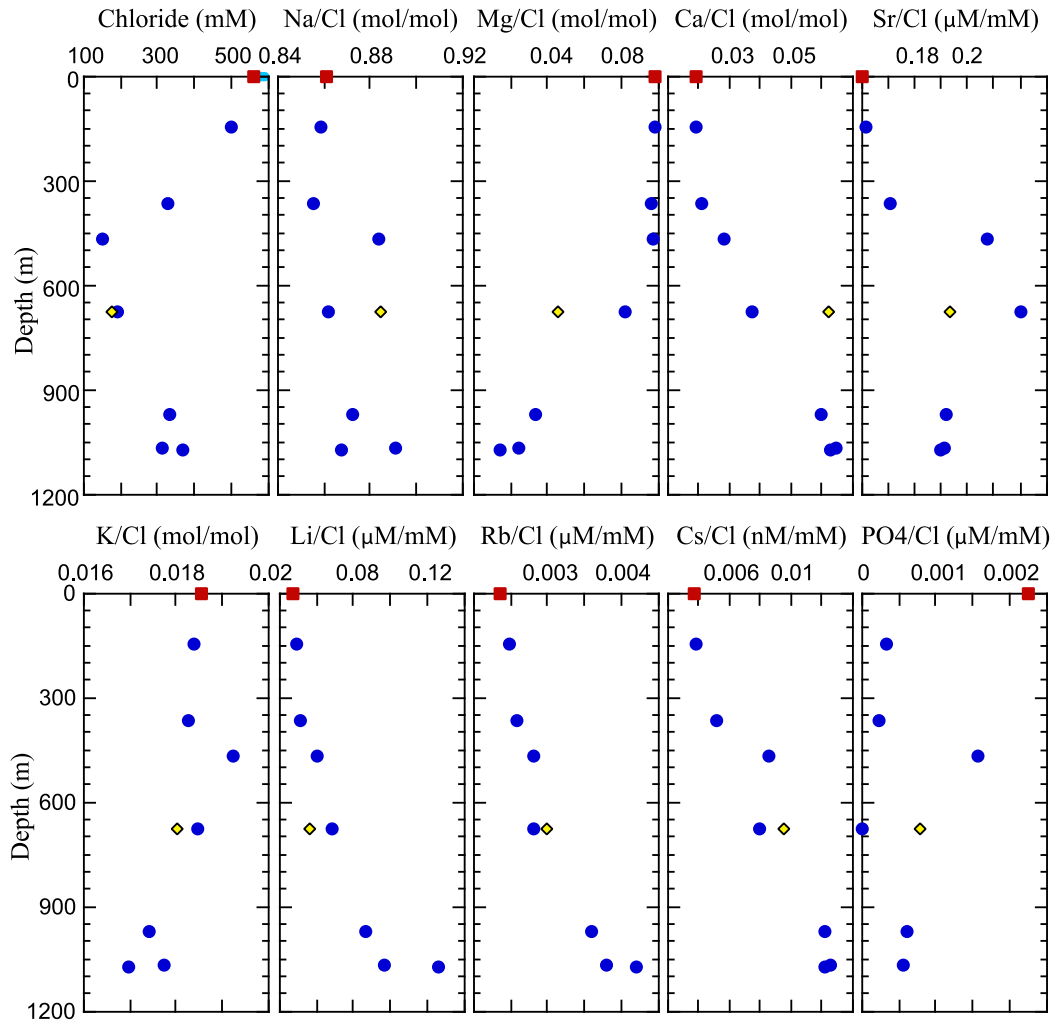

Figure 4. Chloride concentrations and molar ratios (sodium, magnesium, calcium, strontium, potassium, lithium, rubidium, cesium, and phosphate) relative to chloride are plotted as a function of depth (same symbols as in Figure 2). In general, ratios are consistent with those in bottom seawater to ~450 mbsf, then trend to concentrations that are consistent with water-rock reactions. Plots of additional solutes are presented below and in Figure S3 in Supporting Information S1.

Average values and one standard deviation for the fraction of the zero-Mg water based on these five solutes are shown in Figure 6. The fraction of the zero-Mg water is minimal in the upper borehole but increases to ~80% of the water mass in the deepest samples. Similarly, the average fractions of freshwater and seawater were calculated. To show that the calculations are robust, the fraction of freshwater was compared to the Cl data divided by the bottom seawater Cl concentration, since freshwater is almost depleted in Cl and the zero-Mg and seawater Cl concentrations are similar. Similarly, the calculated fraction of seawater was compared to the Mg data divided by the Mg concentration in bottom seawater because the zero-Mg water and freshwater are depleted in Mg.

Fractions of the zero-Mg water were then used to calculate the rate of discharge of the zero-Mg water into the borehole that likely originates deeper than 970 mbsf. We assumed a gradient in the percentage of the zero-Mg water from 0% at 500 mbsf to 80% at the base of the borehole at the time of sampling (1182.2 mbsf; Figure 6). The advective influx of zero-Mg water is 0.06 L/s given the time between the third water sample operation, which captured the deepest sample, and the end of flushing the borehole with fresh water (2.94 days) and a nominal 25.4 cm diameter borehole. At this advective rate, it would take 13 days to flush the 1268-m-deep borehole and is an order of magnitude less than the density-driven mixing calculated in the upper portion of the borehole.

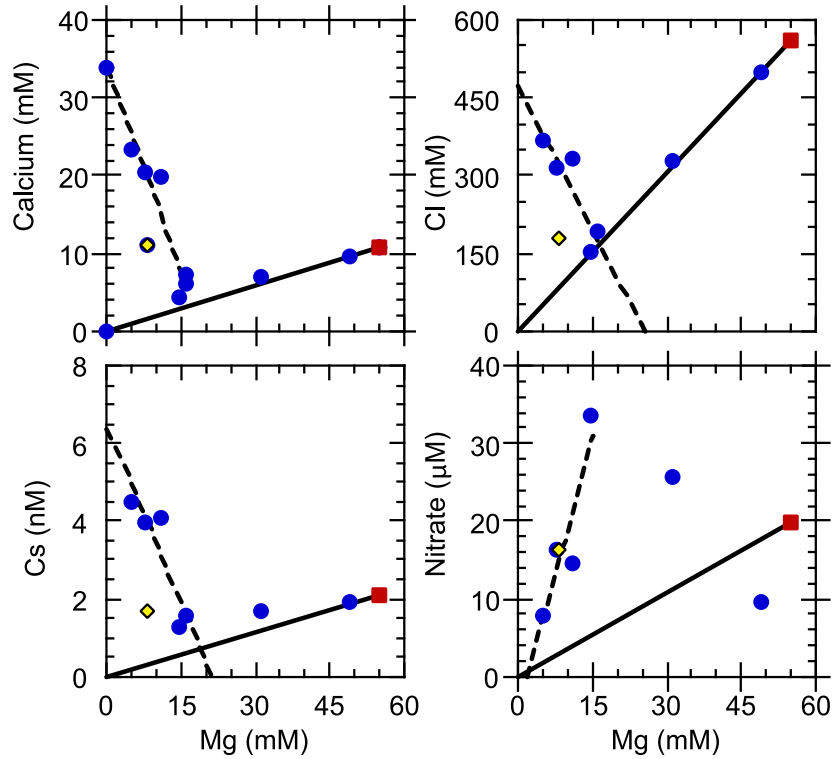

Figure 5. Plots of calcium, cesium, and chloride versus magnesium highlight the three primary sources: freshwater, bottom seawater, and a zero-Mg water. Solid lines reflect conservative mixing between bottom seawater and freshwater. Dashed lines reflect conservative mixing between a 0 mM Mg water and a freshwater/bottom seawater mixture. Some solutes, such as nitrate, do not mix conservatively, indicating reactions within the upper portion of the borehole. Such reactions are fast enough to obfuscate mixing trends documented by the major ions in seawater. Additional solutes are shown in Figure S4 in Supporting Information S1.

4.3. What Is the Source of the Zero-Mg Water?

The major ion geochemistry indicates a 0 mM Mg and high Ca endmember (Table 1); however, only 2.94 days passed between flushing the borehole with freshwater and the third water sample collection. This timeframe is insufficient to reduce the seawater concentrations of Mg to zero solely by reaction within the borehole, given that water-rock experiments at 70°C result in a 13% change in Mg after 150 days (Seyfried and Bishchoff, 1979). Therefore, a component of the zero-Mg water must originate from the rock formation and reflect formation waters that have reacted with host lithologies. This interpretation is consistent with ^{222}Rn and strontium isotope data that reflect the presence of water that has reacted with the rock formation over extended periods of time (Lang, Wheat, et al., 2025).

To deconvolute potential components for the zero-Mg water, we must consider the drilling process. During drilling, surface seawater was extensively pumped into the borehole to flush cuttings. Also, fresh water was pumped into the borehole only days prior to sample collection. Pumping creates an overpressure that could drive these waters, drilling muds, and fine cuttings into permeable formations. Infiltration into the permeable formation was documented in IODP Exp 327 using chemical tracers (Neira et al., 2016). Thus, in Hole U1601C, the zero-Mg water could include components of the natural formation water, surface seawater, and freshwater.

The portion of freshwater that contributes to the zero-Mg water is constrained by the chloride data. The extrapolated concentration of 0 mM Mg is 472 mM Cl, 85% of the bottom seawater concentration. Hydrothermal waters that discharge from LCHF have Cl concentrations that are 2% lower than bottom seawater (Seyfried et al., 2015), which is attributed to the uptake of Cl in serpentinite minerals (Mével, 2003; Sharp and Barnes, 2004) or the dehydration of minerals such as brucite (Seyfried et al., 2015). In Hole U1601C, there are no water-rock reactions that could account for such a substantial loss (15%) of chloride or an equivalent gain in fresh

Table 1
Solute Concentrations, Analytical Methods, and Units for Bottom Seawater (BW), Zero-Mg Water, and Zero-Mg Water Adjusted for Chloride and Sulfate Are Listed and Compared With Hydrothermal Fluid Concentrations From the LCHF (Seyfried et al., 2015)

Solute	Method	Ship/shore	unit	BW	0 Mg 1601C	0 Mg Adj 1601C	LCHF
Nitrate	colorimetric	Shore	µM	19.9	0	0	
Phosphate	colorimetric	Shore	µM	1.26	0	0	
$\delta^{13}C$	MS	Shore	‰	0.21			
$\delta^{18}O$	MS	Shore	‰	0.47	1.39		
Alkalinity	titration	Ship	mM	2.32	0	0	
Br	IC	Ship	mM	0.83	0.71	0.8	0.85
Ca	IC/ICPOES	ship/shore	mM	10.7	34	27.4	27.4
Cl	IC	Ship	mM	559	471	555	541
Na	IC/ICPOES	ship/shore	mM	482	414	488	494
Mg	IC/ICPOES	ship/shore	mM	55	0	0	0
pH	electrode	ship		7.84	7.8		10.6
K	IC/ICPOES	ship/shore	mM	10.4	8	9.4	10.5
Sulfate	IC/ICPOES	ship/shore	mM	28.8	10.8	0	3.2
Sr	ICPOES	Shore	µM	89.6	86	101	102
Ba	ICPOES	Shore	µM	0.048	>1.3		
B	ICPOES	Shore	µM	404	240	283	38
Mn	ICPOES	Shore	µM	<0.1	4.9	8.5	
Fe	ICPOES	Shore	µM	<0.1	0	0	
Li	ICPOES	Shore	µM	26.6	59	69.5	46
Si	ICPOES	Shore	µM	16	100	118	72.7
Rb	ICPMS	Shore	µM	1.32	2.1	2.4	2.8
Cs	ICPMS	Shore	nM	2.1	6.4	7.5	16
Y	ICPMS	Shore	nM	0.3	0.2	0	
Mo	ICPMS	Shore	nM	103	400	440	
U	ICPMS	Shore	nM	12.5	−0.3	0	
Temp (max)	probe	Ship	°C	2			116
Charge Balance	calculate		mM	−5	2	3	−12

water. Thus, the zero-Mg water has a significant freshwater component that affects all solute concentrations, which are adjusted in Table 1.

The zero-Mg water has a sulfate concentration of 10.8 mM, which increases to 12.4 mM, accounting for a 15% dilution with freshwater. If we assume that the formation water is at least 150°C, exceeding the conservative borehole temperature of 140°C (Lang, Wheat, et al., 2025), then the formation water should be void of sulfate, given that anhydrite would precipitate with borehole waters that have elevated Ca concentrations relative to seawater (Bischoff & Seyfried, 1978; Seyfried & Bischoff, 1979).

One possibility is that the formation water is much hotter than 150°C and is devoid of sulfate and that the source of sulfate in the zero-Mg water is from surface seawater that was introduced into the formation during attempts to clear cuttings from the borehole. If we assume sulfate is from surface seawater, then 40% of the zero-Mg water would consist of surface seawater. While this percentage is feasible given the volume of surface seawater that was pumped into the borehole to clear cuttings, it is likely excessive based on previous formation water studies (Neira et al., 2016; Solomon et al., 2009; Wheat et al., 2020). Furthermore, for this scenario to be correct, surface seawater that entered the borehole must react within the borehole to remove Mg and dissolved inorganic carbon

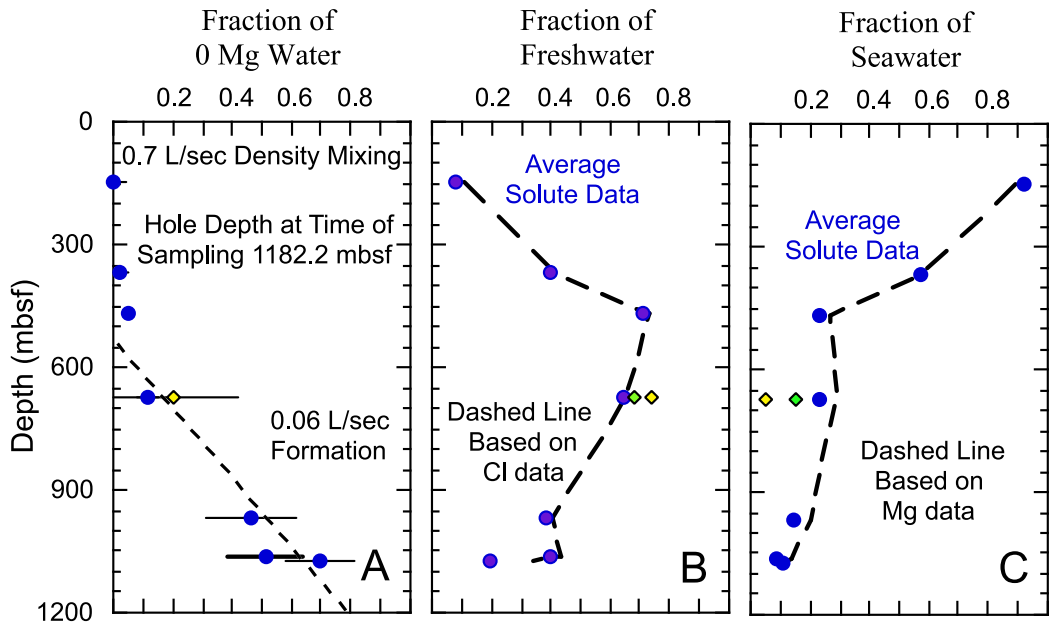

Figure 6. (a) Average and one standard deviation of the fraction of the zero-Mg water calculated from the Ca, sulfate, K, Li, and Rb data. The instantaneous influx of rock-altered water is 0.06 L/s, whereas the density driven mixing is about 0.7 L/s. (b) Fraction of fresh water from the solute data are compared to the Cl data divided by the Cl bottom seawater concentration (dashed line). (c) Fraction of seawater from the solute data are compared to the Mg data (dashed line). Data from the low volume sample from 675 mbsf are shown for comparison (Average of solutes—yellow; either Cl or Mg—green).

(DIC), given that alkalinity measurements indicate DIC is also nearly depleted in formation waters (Lang, Wheat, et al., 2025). Such removal could occur from precipitation of sepiolite, brucite, and/or Mg-carbonate formation (dypingite, hydromagnesite and nesquehonite); however, cation exchange between Mg and Ca is not consistent with the data.

Alternatively, the high sulfate data are consistent with the dissolution of anhydrite/gypsum during sample recovery and handling. These minerals could have formed from seawater-derived sulfate that was introduced to the borehole during drilling operations. Borehole waters from Hole U1309D revealed several samples where anhydrite dissolution occurred after the sample was collected and prior to sample allocation on the ship (McCaig et al., 2024). Particles, including anhydrite, were recovered in the U1309D samples and we have identified gypsum in samples from Hole U1601C (Figures S5–S9 in Supporting Information S1). Using the water-organic-rock-microbe (WORM) thermodynamic workspace (Boyer et al., 2024), anhydrite is at saturation within the borehole at Hole U1601C. Likewise, barite was filtered from borehole water (Figure S6 in Supporting Information S1) and is near saturation throughout the borehole, suggesting that measured Ba concentrations primarily reflect changes in sulfate concentrations. Anhydrite or gypsum dissolution in samples from Hole U1601C provides a coherent explanation for the observed geochemistry, avoiding the Mg and DIC inconsistencies inherent in the alternative scenario.

A likely upper bound for the percentage of surface seawater, which would have been introduced during drilling operations, in the formation is the lowest Mg concentration measured (5.1 mM Mg), resulting in a maximum surface seawater component of 9%. Extrapolating Mg/Cl molar ratios to the base of the borehole during sampling suggests an even lower Mg concentration, resulting in a maximum surface seawater fraction close to 4%. Additional evidence for a minimal impact of surface water on this zero-Mg water is indicated by the water ($\delta^{2}H$, $\delta^{18}O$) isotope data (Figure S10 in Supporting Information S1). Therefore, we consider the formation water to be the zero-Mg water that is adjusted for Cl (15%) and for sulfate and Ca (removal of 12.7 mM Sulfate and Ca after the Cl adjustment) (Table 1).

4.4. Constraints on the Formation Water Temperature

One of the key parameters that defines water isotopic composition after it has reacted with rocks is temperature. The warmest temperature measured in the borehole was 91.3°C at 1060 mbsf, which represents a minimum value as the borehole rebounds from cooling during drilling operations. As noted above, a conservative estimate for the temperature at the base of the borehole is 110–140°C at a depth of 1268 mbsf (Lang, Wheat, et al., 2025). One method to estimate the temperature of water-rock reactions utilizes the $\delta^{18}O$ of water, whose isotopic signal reflects the conditions at which it last equilibrated with host rock. The extent of isotopic exchange between water and rock is governed by temperature and the water-rock ratio (O'Neil and Taylor, 1967; Wenner and Taylor, 1971) and expressed as (Ohmoto and Rye, 1974):

$$1000 \ln \alpha_{\text{rock-fluid}} = \delta^{18}O_{\text{initial rock}} + \left((W/R) \times \delta^{18}O_{\text{seawater}}\right) - \left(\delta^{18}O_{\text{fluid}} \times [1 + (W/R)]\right) \quad (3)$$

where $\alpha_{\text{serp-fluid}}$ is the temperature dependent fractionation factor between the water and rock, W/R is the atomic water to rock ratio, and $\delta^{18}O_{\text{initial rock}}$, $\delta^{18}O_{\text{seawater}}$, and $\delta^{18}O_{\text{fluid}}$ are the oxygen isotopic compositions of the unreacted rock, the initial seawater, and the final reacted water compositions.

Inputs for the equation above can be derived from measured borehole water samples and components from prior studies. For example, the 0 Mg endmember has a $\delta^{18}O$ of 1.39 ‰, based on the two highest purity samples after accounting for contributions from freshwater and seawater (Supplemental Discussion, Table S3, Figures S10 and S11 in Supporting Information S1). The W/R ratio can be estimated using strontium isotope data from borehole waters, which are nearly identical to LCHF hydrothermal fluids (Lang, Wheat, et al., 2025). Previous studies show that LCHF hydrothermal fluids with similar strontium isotope compositions have water-rock mass ratios of approximately 2–4 (Foustoukos et al., 2008). For the initial rock composition, we assume borehole waters reacted with mantle peridotite as the $\delta^{2}H$ of water has values that are above typical mafic-equilibrated values (Figure S11 in Supporting Information S1). We used an initial $\delta^{18}O_{\text{initial rock}}$ of 5.5 ± 0.2 ‰ (Mattey et al., 1994). Applying fractionation factors from Saccocia et al. (2009), where T is temperature in Kelvin:

$$1000 \ln \alpha_{\text{serp-fluid}} = 3.49 \text{ x } 10^{6}/T^{2} - 9.48 \quad (4)$$

results equilibrium temperature of ~350 ± 50°C.

Alternatively, if the $\delta^{18}O$ of the final rock that came into equilibrium with the fluids is known, the equilibration can be calculated directly (Wenner and Taylor, 1971):

$$\alpha_{\text{serp-fluid}} = \left(1 + \delta^{18}O_{\text{rock,final}}/1000\right)/\left(1 + \delta^{18}O_{\text{fluid}}/1000\right) \quad (5)$$

where $\delta^{18}O_{\text{rock, final}}$ is the final equilibrated value of the reacted rock. For example, data from plagioclase-free serpentinite from U1309D has a $\delta^{18}O$ of 3.1 ± 0.4‰ (n = 5; McCaig et al., 2010) and IODP Exp. 357 cores have mesh texture serpentinite with $\delta^{18}O$ of 2.9 ± 0.9‰ (n = 62; Roumejon et al., 2018). Using these values results in temperatures of 300 ± 20°C.

More robust constraints on the equilibration temperatures could be obtained with more sophisticated modeling that would consider multiple mineral types that the fluids may have equilibrated with (e.g., Schmidt et al., 2011; Zakharov et al., 2021), but our simple approach is sufficient to demonstrate that the borehole fluids equilibrated at temperatures at or above the temperatures of discharging LCHF hydrothermal fluids (Früh Green et al., 2003).

4.5. Reactions Within Borehole That Affect Borehole Water Concentrations

In general, plots of solute versus Mg result in two conservative mixing relationships. However, some solutes are so reactive in the borehole that in situ reactions overprint this general mixing trend (e.g., nitrate in Figure 5). For example, nitrate concentrations are higher than expected based on conservative mixing of freshwater and bottom seawater in the upper ~450 m of the borehole, likely a result of microbial nitrification. Other solutes that are commonly used in microbial metabolic processes or influenced by reactions within the borehole (e.g., Mn, Mo, Fe, phosphate, alkalinity, Ba, Si, V, and U) also show non-conservative mixing in the upper borehole (Figure 7; Figures S3 and S4 in Supporting Information S1).

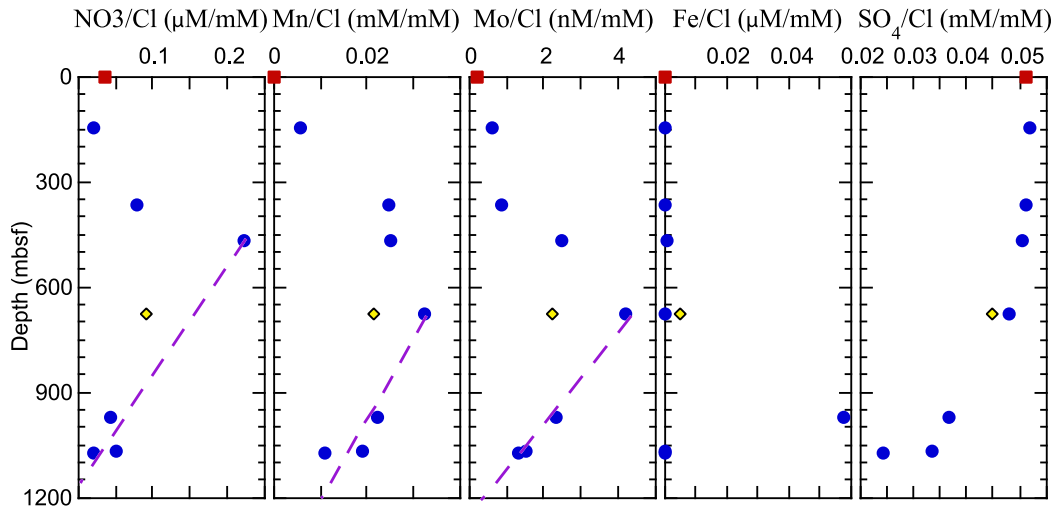

Figure 7. Molar (nitrate, manganese, molybdenum, iron, and sulfate) ratios relative to chloride are plotted as a function of depth for solutes that are typically associated with microbial metabolism. The dashed line represents the potential conservative mixing of a zero-Mg water with a freshwater-seawater mixture. Symbols the same as Figure 2.

Microbial metabolic processes influence the chemical composition of borehole waters more than conservative mixing of the three waters for some solutes. For example, nitrate concentration peak at 30 μM at 465 mbsf, higher than anticipated from dilution with freshwater (Figures 2, 5, and 7). This increase likely results from microbial nitrification of organic matter, that could be enhanced by mixing oxygenated and relatively organic rich bottom seawater with a warm borehole water with H_2 and CH_4 from the borehole walls and formation (Lang, Wheat, et al., 2025). In contrast, below 465 mbsf, dissolved oxygen is likely depleted as nitrate and Mg data are consistent with conservative mixing with a zero-Mg water that is depleted in both solutes (Figure 5).

With the lack of dissolved oxygen below 465 mbsf, Mn, Fe, and sulfate reduction could occur. The peak in the Mn/Cl molar ratio occurs at 675 mbsf, consistent with Mn reduction. Likewise, the Mo/Cl ratios peak at 675 mbsf. For these two solutes, we used the four deepest samples (Figure 7), excluding data from 1075 mbsf, to calculate the concnntrations of both solutes in the zero-Mg water (8.5 and 440 μM, respectively). Fe and sulfate reduction in the borehole are less certain. Fe data show a spike in concentration at 970 mbsf, which could reflect more reducing conditions with depth or could result in a dissolved particle that managed to evade the 0.4-micron filter. While we cannot preclude sulfate reduction, neither the sulfate nor alkalinity data deviate from conservative mixing trends, suggesting that the extent of sulfate reduction, if it occurs, is not significant enough to alter the borehole water composition.

Other solutes also show non-conservative behavior in the borehole. Phosphate, V and U can be scavenged by iron oxides (Feely et al., 1991) in the upper ~465 mbsf of the borehole, where dissolved oxygen likely exists and could support the precipitation of Mn- and Fe-oxides. Concentration trends of all three of these solutes versus Mg data from deeper in the borehole suggest conservative mixing toward a depleted zero-Mg water. The removal of phosphate from the upper portion of the borehole is even more extensive than the borehole trends indicate. Nitrification of organic matter, which generates about a 30 μM nitrate, would release about 2 μM of phosphate to the borehole, assuming a Redfield Ratio. Y is likewise removed in the upper portion of the borehole, but conservative mixing in deeper portions shows an increase in Y but to concentrations less than that of bottom seawater.

In contrast, Si and alkalinity data suggest that both solutes are produced in the upper portion of the borehole (Figure S4 in Supporting Information S1). Increases in Si concentrations are modest (<50 μM) and could reflect several clay-related reactions, which would be below the analytical detection limit for measured cations to confirm such claims; however, the high Si content of the freshwater obfuscates potential trends (Table S1). Likewise, the alkalinity increase is likely related to the dissolution of particles carried with bottom seawater as nitrification tends to decrease alkalinity. The modest increase in alkalinity (0.5 mM) is difficult to discern in the Ca data, although the data do not preclude its occurrence because of carbonate dissolution upon sample recovery and handling, similar to the case for sulfate and Ca described above.

Because of the various potential reactions within the borehole and several potential source components, the basis for some solute data is not straightforward even when coupled with isotope data. For example, the B concentration in the formation water is substantially lower than seawater values, but an order of magnitude higher than LCHF hydrothermal fluids (Table 1). Boron is depleted in hydrothermal fluids from ultramafic-hosted hydrothermal systems, typically ascribed to B uptake during serpentinization (Boschi et al., 2008), while mafic-hosted hydrothermal fluids are enriched in B resulting from high-temperature leaching. Formation waters in U1601C are therefore consistent with a more dominant gabbroic source than a peridotite source, although there is ample evidence for both (e.g., Lang, Wheat, et al., 2025).

Boron isotope compositions of the deepest borehole water samples (δ^{11}B of 37.0–37.1‰) are similar to seawater values (38.8 ‰) but enriched relative to LCHF hydrothermal fluids ($+25 < \delta^{11}B < +30$‰), yet not as enriched as postulated (δ^{11}B up to +120‰) serpentinization-related fluids produced via Rayleigh-type distillation (e.g. Foustoukos et al., 2008) (Figure 2). Borehole B isotope compositions do not change systematically with depth and are likely obfuscated by B uptake or release reactions within the borehole (Figure 2 and Figure S12 in Supporting Information S1). For example, B could be adsorbed onto surface or interlayer sites of sepiolite drill mud or other clay minerals exposed during drilling, scavenged on iron oxides or oxyhydroxides, and/or released from brucite breakdown in fractured rocks. A quantitative assessment of these potential reactions is precluded by the complexity of the borehole hydrology and mixture of suspended material (e.g., Figures S5–S9 in Supporting Information S1). Thus, the B isotopic data do not constrain either the extent of isotopically light B leached from gabbroic lithologies or isotopically fractionated serpentinization-related waters. Thus, B isotope and concentration data, as well as all solute data, need to be re-collected from the borehole, which by now has rebounded from drilling operations, to better constrain the composition of the formation water and the underlying water-rock reactions and conditions.

4.6. Potential Relationship to Lost City Hydrothermal Fluids

Borehole waters from Hole U1601C provide a unique opportunity to constrain the reaction path dynamics at LCHF. Several models have been identified to account for the measured concentrations and isotopes of solutes that discharge at LCHF (e.g., Aquino et al., 2024; Delacour, Früh-Green, Frank, et al., 2008; Evans et al., 2024; Liebmann et al., 2018; Lowell, 2017; McCollom et al., 2016; Seyfried et al., 2015). In general, models start with seawater reactions with mafic and ultramafic rocks at depth followed by conductive cooling and continued reactions with peridotite, consistent with recovered rocks and minerals from U1601C (Lang, McCaig, et al., 2025; Lissenberg et al., 2024). While details of these models differ depending on the chemical data used, the overriding consensus is a multi-compartmentalization of reactions with the first set of reactions primarily involving mafic (gabbroic) rocks at temperatures of 250 ± 50°C. For example, the most recent model presents K isotope values and concentrations that must be derived from mafic rocks of D-MORB (Evans et al., 2024).

Compositions of the formation water from U1601C and LCHF hydrothermal fluids share similar alkali metal concentrations (e.g., Rb, Cs, and K). Both waters have high Li concentrations; however, the projected formation waters have twice the Li concentrations of the LCHF hydrothermal fluids. These high concentrations coupled with Sr and K isotopic compositions point toward reactions with gabbroic rocks (Delacour, Früh-Green, Frank, et al., 2008; Evans et al., 2024; Seyfried et al., 2015), which are increasingly prevalent below 640 mbsf, and are dominant below ~950 mbsf (Lang, McCaig, et al., 2025; Lissenberg et al., 2024). Recovered gabbros and peridotites are extensively altered with at least two phases of alteration: one at relatively high temperature (350–400°C) and the other at lower temperatures (<350°C) (Lissenberg et al., 2024) that includes carbonate vein formation and widespread serpentinization (Foustoukos et al., 2008; Lang, Wheat, et al., 2025).

The Si and Ca data also point toward a gabbroic source. Seyfried et al. (2015) illustrate that peridotite alteration alone cannot account for the elevated Si concentrations in Lost City fluids (Allen & Seyfried, 2004; Frost & Beard, 2007). They propose tremolite-diopside-serpentine-water equilibria at 180–200°C, suggesting that plagioclase is required to account for the observed Si concentrations. Borehole Si concentrations are even higher than those from LCHF but are still undersaturated with respect to quartz and chalcedony at measured temperatures (WORM, Boyer et al., 2024). Similarly, Lissenberg et al. (2024) suggest that Ca is derived from gabbro alteration. Formation waters have identical Ca concentrations (24.7 mM) relative to LCHF hydrothermal fluids. This Ca concentration is less than the calculated concentration of Ca (57.7 mmol/kg) based on reactions between seawater and mafic rocks at 250°C (Evans et al., 2024). The lower pH for mafic reactions, relative to the hydration of

peridotites, supports the higher B concentrations in formation waters relative to hydrothermal waters, but again requires higher temperatures (300°C or more (e.g., Foustoukos et al., 2008)) and contributions from a grabbroic source.

Further evidence of the interaction of rock-altered formation water with gabbroic lithologies comes from Sr isotope data (Lang, Wheat, et al., 2025). Assuming a maximum 9% contribution of Sr from surface seawater ($^{87}Sr/^{86}Sr$ = 0.709193), mass balance indicates that the Sr isotope composition of the deepest sample ($^{87}Sr/^{86}Sr$ = 0.706372) reflects mixing with a rock-altered zero-Mg fluid with a Sr isotope composition ($^{87}Sr/^{86}Sr$~0.7061) lower than endmember LCHF fluid ($^{87}Sr/^{86}Sr$ = 0.7065; Aquino, 2022). Contribution of Sr from dissolution of plagioclase in rubble at the base of the borehole could be an additional source of unradiogenic Sr but requires very high rates of dissolution and upward advection of reacted borehole water. Considering the suite of data, $^{87}Sr/^{86}Sr$ composition of the formation water is very likely to reflect high degrees of fluid-rock reaction likely associated with the alteration of gabbroic rocks, which are typically an order of magnitude higher in Sr than in depleted mantle peridotite (Boschi et al., 2008; Lang, Wheat, et al., 2025).

Consistently, temperatures greater than 200°C are required to account for the observed chemical composition of formation waters extracted from the borehole. At such temperatures, anhydrite would precipitate from seawater (Bischoff & Seyfried, 1978). Given the increase in Ca concentrations above seawater concentrations, anhydrite saturation would occur at lower temperatures (e.g., 140°C, Lang et al., 2012). Thus, sulfate must be removed from the formation water as the intruded seawater warms and reacts with the rock matrix and prior to much hotter (350°C) reactions at depth.

In contrast to the sulfate depleted formation water, the hottest vents at LCHF contain up to 3.7 mM sulfate (Aquino, 2022; Lang et al., 2012; Seyfried et al., 2015), which was interpreted to restrict subseafloor fluid temperatures to 140–190°C based on anhydrite solubility (Lang et al., 2012). However, estimates of subseafloor temperature from LCHF $\delta^{18}O$ data and K isotopes are more consistent with temperatures of 250 ± 50°C (Evans et al., 2024; Foustoukos et al., 2008; Seyfried et al., 2015). This suggests that the sulfate concentrations at LCHF result from the mixing of deep, hot sulfate-depleted formation water with bottom seawater within the rock matrix. This seawater input would have to penetrate well within the rock formation to account for the sulfur isotope composition, which indicates that the source of sulfate in LCHF hydrothermal waters is bottom seawater that has been subjected to closed-system thermochemical sulfate reduction during hydrothermal circulation (Aquino, 2022). For reasons unknown, the precipitation of anhydrite-gypsum, which is not evident in rocks recovered from U1601C or the shallower drill holes recovered on Exp 357 (Früh-Green et al., 2017; Lang, McCaig, et al., 2025; Liebmann et al., 2018), though it is noted in the gabbroic dominated Hole U1309D (Delacour, Früh-Green, & Bernasconi, 2008), does not appear to significantly affect sulfate concentrations during the hydrologic path of LCHF hydrothermal fluids (Aquino, 2022), again suggesting a decoupling from the hot gabbroic source (e.g., borehole water) and the introduction of bottom seawater.

5. Conclusions

IODP Exp 399 drilled an unprecedented section (1268 mbsf, Hole U1601C) of altered peridotites with interlayers of gabbroic material accompanied with H_2, methane, and other hydrocarbons (Lissenberg et al., 2024; Lang, McCaig, et al., 2025; Lang, Wheat, et al., 2025). After drilling operations ceased, waters were collected from the open borehole. Systematic variations in the chemical composition of borehole waters delineate four potential sources: bottom seawater, surface seawater (used to flush cuttings), freshwater (used prior to logging), and a rock-altered water. Freshwater and seawater dominate the borehole water composition in the upper ~465 m of the borehole. The deeper section, however, was dominated by a rock-altered zero-Mg water, which actively discharged into the borehole from permeable zones in the borehole wall. This discharge is consistent with Sr isotopic and ^{222}Ra data as well as H_2 and CH_4 concentrations reaching 100s of μmolar (Lang, Wheat, et al., 2025).

The rock-altered, zero-Mg water is comprised of freshwater and potentially very minor amounts of surface seawater, which were introduced during drilling operations, and formation water, which has high concentrations of Rb, Cs, Si, Ca, and B relative to LCHF hydrothermal fluids, consistent with a significant gabbroic source at temperatures ≥300°C. In addition, there is evidence for reactions with peridotite as is evident from abundant H_2 and CH_4, B and trace metal concentrations that are lower than seawater values, and δ^2H of water that is above mafic-equilibrated values. This finding suggests that the deep-sourced water is a complex mixture of water that

has reacted with gabbro and peridotite, but the current dataset is not sufficient to define reaction mechanisms, equilibrated temperatures, or partitioning between the two rock types; Hole 1601C has the potential to provide pristine formation waters, reflective of a deep-sourced water that is not obfuscated during the tortuous path to the seafloor. Distinguishing the balance of gabbroic and peridotite influenced reactions in this study was complicated because of the multiple sources. Even though borehole waters were collected only days after drilling operations ceased, they clearly show the chemical imprint from deep-sourced reactions and active discharge into the borehole. Future sampling of pristine borehole waters would allow us to, for example, measure (a) pH values (gabbroic host rocks should have lower pH values), (b) trace metal concentrations that are unaffected by oxygenated seawater and freshwater, leading to a better understanding of subsurface processes, (c) concentrations of dissolved gases using gas-tight samplers, including H_2, which is critical to establishing reaction mechanisms, and (d) dissolved organics in a simplified matrix of water types and particles. Such new data will provide valuable insights into how shallow and deep reactions within the rock formation influence the production and consumption of organics and solutes for microbial consumption and their impact on geochemical fluxes and alteration of near surface lithologies.

Conflict of Interest

The authors declare no conflicts of interest relevant to this study.

Availability Statement

Data files used in this paper are available in McCaig et al. (2024), in the Supporting Information of this paper, and https://doi.org/10.5281/zenodo.18364583.

Acknowledgments

We thank the dedicated captain and crew of the JOIDES Resolution for aiding in sample collection and the review process that improved this manuscript. Funding: This research used samples and data provided by the International Ocean Discovery Program (IODP). Funding for the operation and management of the scientific drilling vessel JOIDES Resolution was provided by the US National Science Foundation (NSF) (award OCE, 1326927). Funding to join Expedition 399 was provided by NSF (Grant OCE, 1450528) for the US Science Support Program Office associated with the International Ocean Discovery Program [USSSP-IODP subcontract 22O (GG009393-04) to S.Q.L., K.L.D., and C. G.W., and Australia New Zealand International Consortium (ANZIC) IODP (to G.S.). Shore-based analytical work was supported by USSSP-IODP subcontract 22O(GG009393-04) to S.Q.L and C.G.W., EPOS JRU ITALIA, and UK Natural Environment Research Council (NERC) NE/Y002415/1 to I.P.S.

References

Agostini, S., Di Giuseppe, P., Manetti, P., Doglioni, C., & Conticelli, S. (2021). A heterogeneous subcontinental mantle under the African-Arabian Plate boundary revealed by boron and radiogenic isotopes. *Scientific Reports*, *11*(1), 11230. https://doi.org/10.1038/s41598-021-90275-7

Allen, D. E., & Seyfried, W. E., Jr. (2004). Serpentinization and heat generation: Constraints from Lost City and Rainbow hydrothermal systems. *Geochimica et Cosmochimica Acta*, *68*(6), 1347–1354. https://doi.org/10.1016/j.gca.2003.09.003

Alt, J. C., Honnorez, J., Laverne, C., & Emmermann, R. (1986). Hydrothermal alteration of a 1 km section through the upper oceanic crust, Deep Sea Drilling Project Hole 504B: Mineralogy, chemistry and evolution of seawater-basalt interactions. *Journal of Geophysical Research*, *91*(B10), 10309–10335. https://doi.org/10.1029/jb091ib10p10309

Aquino, K. A. (2022). Fluid mixing and spatial geochemical variability in the Lost City hydrothermal field chimneys (research data) [Dataset]. *ETHZ Research Collection*. https://doi.org/10.3929/ethz-b-000579720

Aquino, K. A., Früh-Green, G. L., Bernasconi, S. M., Rickli, J., Lang, S. Q., & Lilley, M. D. (2024). Fluid mixing and spatial geochemical variability in the Lost City hydrothermal field chimneys. *Geochemistry, Geophysics, Geosystems*, *25*(2), e2023GC011011. https://doi.org/10.1029/2023gc011011

Bischoff, J. L., & Seyfried, W. E. (1978). Hydrothermal chemistry of seawater from 25 degrees to 350 degrees C. *American Journal of Science*, *278*(6), 838–860. https://doi.org/10.2475/ajs.278.6.838

Blackman, D. K., Ildefonse, B., John, B. E., Ohara, Y., Miller, D. J., Abe, N., et al. (2011). Drilling constraints on lithospheric accretion and evolution at Atlantis Massif, Mid-Atlantic Ridge 30 N. *Journal of Geophysical Research*, *116*(B7), B07103. https://doi.org/10.1029/2010JB007931

Blackman, D. K., Ildefonse, B., John, B. E., Ohara, Y., Miller, D. J., MacLeod, C. J., & the Expedition 304/305 Scientists. (2006). *Proceedings of the integrated Ocean Drilling Program, 304/305*. Integrated Ocean Drilling Program Management International, Inc. https://doi.org/10.2204/iodp.proc.304305.2006

Blackman, D. K., Slagle, A., Guerin, G., & Harding, A. (2014). Geophysical signatures of past and present hydration within a young oceanic core complex. *Geophysical Research Letters*, *41*(4), 1179–1186. https://doi.org/10.1002/2013gl058111

Boschi, C., Dini, A., Fruh-Green, G. L., & Kelley, D. S. (2008). Isotopic and element exchange during serpentinization and metasomatism at the Atlantis Massif (MAR 30 degrees N): Insights from B and Sr isotope data. *Geochimica et Cosmochimica Acta*, *72*(7), 1801–1823. https://doi.org/10.1016/j.gca.2008.01.013

Boyer, G., Robare, J., Park, N., Ely, T., & Shock, E. (2024). *AqEquil: Python package for aqueous geochemical speciation (v0.19.0)*. Zenodo. https://doi.org/10.5281/zenodo.13530217

Carlson, R. L. (2010). How crack porosity and shape control seismic velocities in the upper oceanic crust: Modeling downhole logs from Holes 504B and 1256D. *Geochemistry, Geophysics, Geosystems*, *11*(4), Q04007. https://doi.org/10.1029/2009gc002955

Catanzaro, E. J. (1970). *Boric acid: isotopic and assay standard reference materials* (Vol. 260, No. 17). National Bureau of Standards, Institute for Materials Research.

Delacour, A., Früh-Green, G. L., & Bernasconi, S. M. (2008). Sulfur mineralogy and geochemistry of serpentinites and gabbros of the Atlantis Massif (IODP Site U1309). *Geochimica et Cosmochimica Acta*, *72*(20), 5111–5127. https://doi.org/10.1016/j.gca.2008.07.018

Delacour, A., Früh-Green, G. L., Frank, M., Gutjahr, M., & Kelley, D. S. (2008). Sr- and Nd-isotope geochemistry of the Atlantis Massif (30°N, MAR): Implications for fluid fluxes and lithospheric heterogeneity. *Chemical Geology*, *254*(1–2), 19–35. https://doi.org/10.1016/j.chemgeo.2008.05.018

Escartín, J., Smith, D. K., Cann, J., Schouten, H., Langmuir, C. H., & Escrig, S. (2008). Central role of detachment faults in accretion of slow-spreading oceanic lithosphere. *Nature*, *455*(7214), 790–794. https://doi.org/10.1038/nature07333

Evans, G. N., Charin, S., Seyfried, W. E., Jr., & Zheng, X. Y. (2024). The role of mafic intrusions in producing Alkaline vent fluids at the Lost city hydrothermal field: Evidence from stable Potassium Isotopes. *Geochimica et Cosmochimica Acta*, *386*, 84–95. https://doi.org/10.1016/j.gca.2024.08.030

Feely, R. A., Trefry, J. H., Massoth, G. J., & Metz, S. (1991). A comparison of the scavenging of phosphorus and arsenic from seawater by hydrothermal iron oxyhydroxides in the Atlantic and Pacific Oceans. *Deep-Sea Research, Part A: Oceanographic Research Papers*, *38*(6), 617–623. https://doi.org/10.1016/0198-0149(91)90001-v

Foustoukos, D. I., Savov, I. P., & Janecky, D. R. (2008). Chemical and isotopic constraints on water/rock interactions at the Lost City hydrothermal field, 30 N Mid-Atlantic Ridge. *Geochimica et Cosmochimica Acta*, *72*(22), 5457–5474. https://doi.org/10.1016/j.gca.2008.07.035

Frost, B. R., & Beard, J. S. (2007). On silica activity and serpentinization. *Journal of Petrology*, *48*(7), 1351–1368. https://doi.org/10.1093/petrology/egm021

Früh-Green, G. L., Orcutt, B. N., Green, S. L., Cotterill, C., Morgan, S., Akizawa, N., et al. (2017). Proceedings of the Ocean Discovery Program, 357.

Früh-Green, G. L., Orcutt, B. N., Rourméjon, S., Lilley, M. D., Morono, Y., Cotterill, C., et al. (2018). Magmatism, serpentinization and life: Insights through drilling the Atlantis Massif (IODP Expedition 357). *Lithos*, *323*, 137–155. https://doi.org/10.1016/j.lithos.2018.09.012

Früh-Green, G. L., Kelley, D. S., Bernasconi, S. M., Karson, J. A., Ludwig, K. A., Butterfield, D. A., et al. (2003). 30,000 years of hydrothermal activity at the Lost City vent field. *Science*, *301*(5632), 495–498. https://doi.org/10.1126/science.1085582

Gilbert, L. A., & Salisbury, M. H. (2011). Oceanic crustal velocities from laboratory and logging measurements of Integrated Ocean Drilling Program Hole 1256D. *Geochemistry, Geophysics, Geosystems*, *12*(9). https://doi.org/10.1029/2011gc003750

Gillis, K. M., Snow, J. E., Klaus, A., Abe, N., Adrião, Á. B., Akizawa, N., et al. (2014). Primitive layered gabbros from fast-spreading lower oceanic crust. *Nature*, *505*(7482), 204–207. https://doi.org/10.1038/nature12778

Harding, A. J., Arnulf, A. F., & Blackman, D. K. (2016). Velocity structure near IODP Hole U1309D, Atlantis Massif, from waveform inversion of streamer data and borehole measurements. *Geochemistry, Geophysics, Geosystems*, *17*(6), 1990–2014. https://doi.org/10.1002/2016gc006312

Ildefonse, B., Blackman, D. K., John, B. E., Ohara, Y., Miller, D. J., & MacLeod, C. J. (2007). Oceanic core complexes and crustal accretion at slow-spreading ridges. *Geology*, *35*(7), 623–626. https://doi.org/10.1130/g23531a.1

Kelley, D. S., Karson, J. A., Fruh-Green, G. L., Yoerger, D. R., Shank, T. M., Butterfield, D. A., et al. (2005). A serpentinite-hosted ecosystem: The Lost City hydrothermal field. *Science*, *307*(5714), 1428–1434. https://doi.org/10.1126/science.1102556

Lang, S. Q., Früh-Green, G. L., Bernasconi, S. M., Lilley, M. D., Proskurowski, G., Méhay, S., & Butterfield, D. A. (2012). Microbial utilization of abiogenic carbon and hydrogen in a serpentinite-hosted system. *Geochimica et Cosmochimica Acta*, *92*, 82–99. https://doi.org/10.1016/j.gca.2012.06.006

Lang, S. Q., McCaig, A. M., Blum, P., Abe, N., Brazelton, W., Coltat, R., et al. (2025). Site U1601. In A. M. McCaig, S. Q. Lang, P. Blum, & the Expedition 399 Scientists, Building Blocks of Life, Atlantis Massif (Eds.), *Proceedings of the International Ocean Discovery Program, 399*. International Ocean Discovery Program. https://doi.org/10.14379/iodp.proc.399.104.2025

Lang, S. Q., Wheat, C. G., Dickerson, K. L., Reagan, M. K., Savov, I. P., Robare, J. A., et al. (2025). Hydrogen, single-carbon compounds, and thermal regime in the oceanic ultramafic-dominated lithosphere: insights from a deep borehole on the Atlantis Massif. *Geochimica et cosmochimica acta*, *408*, 84–104. https://doi.org/10.1016/j.gca.2025.09.024

Liebmann, J., Schwarzenbach, E. M., Früh-Green, G. L., Boschi, C., Rouméjon, S., Strauss, H., et al. (2018). Tracking water-rock interaction at the Atlantis Massif (MAR, 30°N) using sulfur geochemistry. *Geochemistry, Geophysics, Geosystems*, *19*(11), 4561–4583. https://doi.org/10.1029/2018gc007813

Ligi, M., Bonatti, E., Cuffaro, M., & Brunelli, D. (2013). Post-Mesozoic rapid increase of seawater Mg/Ca due to enhanced mantle-seawater interaction. *Scientific Reports*, *3*(1), 2752. https://doi.org/10.1038/srep02752

Lissenberg, C. J., McCaig, A. M., Lang, S. Q., Blum, P., Abe, N., Brazelton, W. J., et al. (2024). A long section of serpentinized depleted mantle peridotite. *Science*, *385*(6709), 623–629. https://doi.org/10.1126/science.adp1058

Lowell, R. P. (2017). A fault-driven circulation model for the Lost City hydrothermal field. *Geophysical Research Letters*, *44*(6), 2703–2709. https://doi.org/10.1002/2016gl072326

Magenheim, A. J., & Gieskes, J. M. (1996). Simulation of borehole fluid mixing on the basis of geochemical observations, Hole 504B. In *Proceedings-Ocean Drilling Program Scientific Results* (pp. 111–118). National Science Foundation.

Mattey, D., Lowry, D., & Macpherson, C. (1994). Oxygen isotope composition of mantle peridotite. *Earth and Planetary Science Letters*, *128*(3–4), 231–241. https://doi.org/10.1016/0012-821x(94)90147-3

McCaig, A., Lang, S. Q., Blum, P., Abe, N., Brazelton, W., Coltat, R., et al. (2024). International Ocean Discovery Program Expedition 399 preliminary report; building blocks of life, Atlantis Massif; 12 April-12 June 2023. In *Preliminary Report-International Ocean Discovery Program, 399*.

McCaig, A. M., Delacour, A., Fallick, A. E., Castelain, T., & Früh-Green, G. L. (2010). Detachment fault control on hydrothermal circulation systems: Interpreting the subsurface beneath the TAG hydrothermal field using the isotopic and geological evolution of oceanic core complexes in the Atlantic. *Geophysical Monograph Series*, *188*, 207–239.

McCaig, A. M., Titarenko, S. S., Savov, I. P., Cliff, R. A., Banks, D., Boyce, A., & Agostini, S. (2018). No significant boron in the hydrated mantle of most subducting slabs. *Nature Communications*, *9*(1), 4602. https://doi.org/10.1038/s41467-018-07064-6

McCollom, T. M., Klein, F., Robbins, M., Moskowitz, B., Berquó, T. S., Jöns, N., et al. (2016). Temperature trends for reaction rates, hydrogen generation, and partitioning of iron during experimental serpentinization of olivine. *Geochimica et Cosmochimica Acta*, *181*, 175–200. https://doi.org/10.1016/j.gca.2016.03.002

Mével, C. (2003). Serpentinization of abyssal peridotites at mid-ocean ridges. *Comptes Rendus Geoscience*, *335*(10–11), 825–852. https://doi.org/10.1016/j.crte.2003.08.006

Michibayashi, K., Tominaga, M., Ildefonse, B., & Teagle, D. A. (2019). What lies beneath the formation and evolution of oceanic lithosphere. *Oceanography*, *32*(1), 138–149. https://doi.org/10.5670/oceanog.2019.136

Mottl, M. J., & Gieskes, J. M. (1990). Chemistry of waters sampled from oceanic basement boreholes, 1979–1988. *Journal of Geophysical Research*, *95*(B6), 9327–9342. https://doi.org/10.1029/jb095ib06p09327

Neira, N. M., Clark, J. F., Fisher, A. T., Wheat, C. G., Haymon, R. M., & Becker, K. (2016). Cross-hole tracer experiment reveals rapid fluid flow and low effective porosity in the upper oceanic crust. *Earth and Planetary Science Letters*, *450*, 355–365. https://doi.org/10.1016/j.epsl.2016.06.048

Ohmoto, H., & Rye, R. O. (1974). Hydrogen and oxygen isotopic compositions of fluid inclusions in the Kuroko deposits, Japan. *Economic Geology*, *69*(6), 947–953. https://doi.org/10.2113/gsecongeo.69.6.947

O'Neil, J. R., & Taylor, H. P., Jr. (1967). The oxygen isotope and cation exchange chemistry of feldspars. *American Mineralogist: Journal of Earth and Planetary Materials*, *52*(9–10), 1414–1437.

Pariso, J. E., Rommevaux, C., & Sempere, J. C. (1996). Three-dimensional inversion of marine magnetic anomalies: Implications for crustal accretion along the Mid-Atlantic Ridge (28–31 30′N). *Marine Geophysical Researches*, *18*(1), 85–101. https://doi.org/10.1007/bf00286204

Rouméjon, S., Williams, M. J., & Früh-Green, G. L. (2018). In-situ oxygen isotope analyses in serpentine minerals: Constraints on serpentinization during tectonic exhumation at slow-and ultraslow-spreading ridges. *Lithos*, *323*, 156–173. https://doi.org/10.1016/j.lithos.2018.09.021

Saccocia, P. J., Seewald, J. S., & Shanks, W. C., III. (2009). Oxygen and hydrogen isotope fractionation in serpentine–water and talc–water systems from 250 to 450 C, 50 MPa. *Geochimica et Cosmochimica Acta*, *73*(22), 6789–6804. https://doi.org/10.1016/j.gca.2009.07.036

Schmidt, K., Garbe-Schonberg, D., Koschinsky, A., Strauss, H., Jost, C. L., Klevenz, V., & Koniger, P. (2011). Fluid elemental and stable isotope composition of the Nibelungen hydrothermal field (8°18′S, Mid-Atlantic Ridge): Constraints on fluid-rock interaction in heterogenous lithosphere. *Chemical Geology*, *280*(1–2), 1–18. https://doi.org/10.1016/j.chemgeo.2010.07.008

Seyfried, W. E., Jr., & Bischoff, J. L. (1979). Low temperature basalt alteration by sea water: An experimental study at 70 C and 150 C. *Geochimica et Cosmochimica Acta*, *43*(12), 1937–1947. https://doi.org/10.1016/0016-7037(79)90006-1

Seyfried, W. E., Jr., Pester, N. J., Tutolo, B. M., & Ding, K. (2015). The Lost City hydrothermal system: Constraints imposed by vent fluid chemistry and reaction path models on subseafloor heat and mass transfer processes. *Geochimica et Cosmochimica Acta*, *163*, 59–79. https://doi.org/10.1016/j.gca.2015.04.040

Sharp, Z. D., & Barnes, J. D. (2004). Water-soluble chlorides in massive seafloor serpentinites: A source of chloride in subduction zones. *Earth and Planetary Science Letters*, *226*(1–2), 243–254. https://doi.org/10.1016/j.epsl.2004.06.016

Solomon, E. A., Kastner, M., Wheat, C. G., Jannasch, H., Robertson, G., Davis, E. E., & Morris, J. D. (2009). Long-term hydrogeochemical records in the oceanic basement and forearc prism at the Costa Rica subduction zone. *Earth and Planetary Science Letters*, *282*(1–4), 240–251. https://doi.org/10.1016/j.epsl.2009.03.022

Tonarini, S., Pennisi, M., & Leeman, W. P. (1997). Precise boron isotopic analysis of complex silicate (rock) samples using alkali carbonate fusion and ion-exchange separation. *Chemical Geology*, *142*(1–2), 129–137. https://doi.org/10.1016/s0009-2541(97)00087-9

Wenner, D. B., & Taylor, H. P., Jr. (1971). Temperatures of serpentinization of ultramafic rocks based on O18/O16 fractionation between coexisting serpentine and magnetite. *Contributions to Mineralogy and Petrology*, *32*(3), 165–185. https://doi.org/10.1007/bf00643332

Wheat, C. G., Becker, K., Villinger, H., Orcutt, B. N., Fournier, T., Hartwell, A., & Paul, C. (2020). Subseafloor cross-hole tracer experiment reveals hydrologic properties, heterogeneities, and reactions in slow-spreading oceanic crust. *Geochemistry, Geophysics, Geosystems*, *21*(1), e2019GC008804. https://doi.org/10.1029/2019gc008804

Wheat, C. G., Jannasch, H. W., Kastner, M., Plant, J. N., DeCarlo, E. H., & Lebon, G. (2004). Venting formation fluids from deep sea boreholes in a ridge flank setting: ODP Sites 1025 and 1026. *Geochemistry, Geophysics, Geosystems*, *5*(8), Q08007. https://doi.org/10.1029/2004GC000710

Zakharov, D. O., Tanaka, R., Butterfield, D. A., & Nakamura, E. (2021). A new insight into seawater-basalt exchange reactions based on combined $\delta^{18}O$—$\Delta'^{17}O$—$^{87}Sr/^{86}Sr$ values of hydrothermal fluids from the axial seamount volcano, Pacific Ocean. *Frontiers in Earth Science*, *9*, 691699. https://doi.org/10.3389/feart.2021.691699

References From the Supporting Information

Brand, W. A., Coplen, T. B., Vogl, J., Rosner, M., & Prohaska, T. (2014). Assessment of international reference materials for isotope-ratio analysis (IUPAC Technical Report). *Pure and Applied Chemistry*, *86*(3), 425–467. https://doi.org/10.1515/pac-2013-1023